

The Effect of Dissolved Oxygen on the Susceptibility of Blood

Avery J.L. Berman,^{1,2*} Yuhan Ma,¹ Richard D. Hoge,^{3,4} and G. Bruce Pike²

Purpose: It has been predicted that, during hyperoxia, excess O₂ dissolved in arterial blood will significantly alter the blood's magnetic susceptibility. This would confound the interpretation of the hyperoxia-induced blood oxygenation level-dependent signal as arising solely from changes in deoxyhemoglobin. This study, therefore, aimed to determine how dissolved O₂ affects the susceptibility of blood.

Theory and Methods: We present a comprehensive model for the effect of dissolved O₂ on the susceptibility of blood and compare it with another recently published model, referred to here as the ideal gas model (IGM). For validation, distilled water and samples of bovine plasma were oxygenated over a range of hyperoxic O₂ concentrations and their susceptibilities were determined using multiecho gradient echo phase imaging.

Results: In distilled water and plasma, the measured changes in susceptibility were very linear, with identical slopes of 0.062 ppb/mm Hg of O₂. This change was dramatically less than previously predicted using the IGM and was close to that predicted by our model. The primary source of error in the IGM is the overestimation of the volume fraction occupied by dissolved O₂.

Conclusion: Under most physiological conditions, the susceptibility of dissolved O₂ can be disregarded in MRI studies employing hyperoxia. **Magn Reson Med 000:000–000, 2015.** © 2015 Wiley Periodicals, Inc.

Key words: susceptibility; dissolved O₂; blood; BOLD; hyperoxia

INTRODUCTION

The magnetic susceptibility of materials and tissues is of fundamental importance in NMR and MRI. It relates the magnetization induced in matter to an applied external field, and differences in susceptibility across boundaries can produce nonlocal field offsets that alter the MR signal. The susceptibility of hemoglobin (Hb) is of particular significance because the molecule undergoes conformational changes and electronic rearrangement

when binding O₂, which result in a conversion of Hb from being paramagnetic in the deoxygenated state to diamagnetic when oxygenated (1). This property of Hb has been exploited in several MRI techniques, most notably blood oxygenation level-dependent (BOLD) functional MRI (fMRI) for the localization of changing neural activity (2–4) and susceptibility-weighted imaging for the identification of veins (5). These techniques are made possible by the fact that, under normal physiological conditions, Hb in veins and capillaries is partially saturated with O₂, making these vessels paramagnetic relative to the surrounding tissue, which results in frequency offsets between the vessels and tissue and increased transverse decay (6). On the other hand, Hb in arteries under normal physiological conditions generally is nearly fully oxygen saturated, imparting little susceptibility difference relative to the surrounding tissue, and therefore negligible contributions to BOLD fMRI and susceptibility-weighted imaging (neglecting inflow enhancement effects).

Some fMRI techniques now use hyperoxia as a means of altering the BOLD signal. Under hyperoxia, the partial pressure of O₂ (pO₂) in blood is high enough that nearly all arterial Hb is oxygenated and an excess of O₂ molecules are dissolved in arterial blood (7). The excess O₂ in arterial blood that is not consumed by tissue metabolism ends up bound to Hb in veins, reducing the venous concentration of deoxy-Hb (dHb) and resulting in a subsequent increase in the BOLD signal relative to normoxia (breathing of room air). By modulating the BOLD signal, hyperoxia has been used in calibrated BOLD (8,9) and has also been proposed as a method for measuring deoxygenated cerebral blood volume (10).

Being a paramagnetic molecule, O₂ can have significant effects on MR images. It creates large susceptibility differences between air cavities and tissue and in turn can lead to extensive areas of signal dropout in T₂*-weighted images and geometric distortion in echo-planar imaging. It has also been shown to produce aberrant T₂* fluctuations during hyperoxia in brain regions fairly distal to the airways (11) and in peripheral vascular reactivity BOLD studies employing air-pressurized cuffs, even in slices up to 15 cm away from the cuff (12). Despite these effects of gaseous O₂, the susceptibility of dissolved O₂ in blood is commonly ignored during normoxia because the amount dissolved in plasma is normally very small and its contribution to the net susceptibility of blood is negligible compared to that of the other major constituents, specifically oxygenated and deoxygenated red blood cells (RBCs) and plasma (13–15).

Recently, Schwarzbauer and Deichmann (SD) extended the model of the susceptibility of blood to include

¹McConnell Brain Imaging Centre, Montreal Neurological Institute, McGill University, Montreal, Quebec, Canada.

²Department of Radiology and Hotchkiss Brain Institute, University of Calgary, Calgary, Alberta, Canada.

³Institut de génie biomédical, Département de physiologie, Université de Montréal, Montréal, Québec, Canada.

⁴Unité de neuroimagerie fonctionnelle, Centre de recherche de l'institut de gériatrie de Montréal, Montreal, Quebec, Canada

*Correspondence to: Avery Berman, 3330 Hospital Drive NW, HMRB Room 193, Calgary, AB Canada T2N 4N1. E-mail: avery.berman@mail.mcgill.ca

Received 12 August 2014; revised 30 October 2014; accepted 14 November 2014

DOI 10.1002/mrm.25571

Published online 00 Month 2015 in Wiley Online Library (wileyonlinelibrary.com).

© 2015 Wiley Periodicals, Inc.

Table 1
Susceptibility Values Including Their Sources and Their Conversion to Volume Susceptibility in SI Units

Substance	Symbol	Source (ppm, cgs units)	Conversion Factor	$\chi(22\text{ }^\circ\text{C})$ (ppm, SI units)	$\chi(37\text{ }^\circ\text{C})$ (ppm, SI units)
Water	$\chi_{\text{H}_2\text{O}}$	-12.96 cm ³ /mol (34)	Eq. [B.1]	-9.022	-9.001
Oxygen	χ_{O_2}	3415 cm ³ /mol (34)	$\times 4\pi \cdot 293.15\text{ K}/(T + 273.15)/$ $\bar{v}_{M,\text{O}_2:\text{H}_2\text{O}}(T)^b$	1383	1342
Hemoglobin (diamagnetic component)	χ_{diamHb}^a	-0.587 cm ³ /g (13)	$\times 4\pi \cdot 5.5 \times 10^{-6}\text{ mol}/\text{cm}^3 \cdot$ 64450 g/mol (13)	-2.61	-2.61
Plasma proteins	χ_{prot}^a	-0.587 cm ³ /g (13)	$\times 4\pi/0.730\text{ cm}^3/\text{g}$ (19)	-10.1	-10.1
Difference between deoxygenated and oxygenated RBC	$\Delta\chi_{\text{do}}$	0.27 (13,32)	$\times 4\pi \cdot 310.15\text{ K}/(T + 273.15)$	3.57	3.39

SI, International System of Units.

All sources were in cgs units.

^aAside from H₂O, the molar susceptibilities of the diamagnetic molecules were assumed to be temperature-independent (15).

^b $\bar{v}_{M,\text{O}_2:\text{H}_2\text{O}}$ is the partial molar volume of O₂ dissolved in water (see Appendix A for more details).

dissolved O₂ (16). SD theoretically predicted that when concentrations of dissolved O₂ in blood were sufficiently high, such as during hyperoxia, dissolved O₂ would significantly contribute to the susceptibility difference between arterial blood and the surrounding tissue. Using their extended model and simulations, they predicted that in going from normoxia to hyperoxia, MR signal changes from tissues populated by arteries could be substantial and even comparable to venous-driven BOLD contrast. Considering that BOLD studies are geared toward measuring changes in dHb and not dissolved O₂ directly, the implications of SD's findings for fMRI studies using hyperoxia, such as calibrated BOLD, are profound and have led us to reexamine the model of the susceptibility of dissolved O₂ proposed by SD.

In this article, we show that the model used by SD for incorporating the effect of dissolved O₂ into the susceptibility of blood was inaccurate, specifically, the volume fraction of dissolved O₂ was significantly overestimated. We present an alternative model that corrects for this overestimation and have validated it by measuring the effect of increasing levels of dissolved O₂ on the susceptibility of distilled water and ex vivo bovine plasma.

THEORY

Unless stated otherwise, all susceptibilities are volume susceptibilities in the International System of Units (SI); however, several original sources used cgs units, and the susceptibility is often expressed as molar or mass susceptibility. Table 1 and Appendix B describe all of the susceptibility values used throughout this article, including their original sources and their conversion to volume susceptibility in SI units.

For a mixture of substances in solution such as in blood, the net susceptibility of the solution, χ_{net} , is given by the weighted sum of the individual susceptibilities, χ_i ,

$$\chi_{\text{net}} = \sum_i \alpha_i \chi_i, \quad [1]$$

where the weighting factors, α_i , are the volume fractions occupied by the substances in solution. Applying this to blood, χ_{blood} can be divided into contributions from RBCs and plasma (13),

$$\chi_{\text{blood}} = \text{Hct} \cdot \chi_{\text{RBC}} + (1 - \text{Hct}) \cdot \chi_{\text{plasma}}, \quad [2]$$

where Hct is the hematocrit; χ_{RBC} includes contributions from intracellular water, paramagnetic dHb, and diamagnetic oxy-Hb; and χ_{plasma} includes contributions from water and plasma proteins.

To account for dissolved O₂, SD divided χ_{blood} into contributions from O₂, with a volume fraction α_{O_2} , and from RBCs and plasma, with a volume fraction $(1 - \alpha_{\text{O}_2})$. For the volume fraction of O₂, they used $\alpha_{\text{O}_2} = \varepsilon \cdot p_{\text{O}_2}$, where ε is the Bunsen solubility coefficient of O₂ in blood, which was taken to be 3.1×10^{-5} mL O₂/mL blood/mm Hg (7). Crucially, this quantity, $\varepsilon \cdot p_{\text{O}_2}$, is the volume that O₂ in blood would occupy as an ideal gas at standard temperature and pressure (STP) per mL of blood, it is *not* the physical volume fraction occupied by O₂ in blood (17). In fact, when O₂ dissolves in a liquid such as blood or water, the volume occupied by the O₂ in solution is orders of magnitude less than the volume occupied by the same number of moles in the gaseous state at STP. Additionally, in this model, the contribution of dissolved O₂ to χ_{blood} is only valid for an average Hb concentration (and therefore Hct) (17). However, the amount of O₂ that can be dissolved in blood is proportional to the amount of blood water, which in turn is dictated by Hct because it displaces plasma—the largest source of blood water. Therefore, SD's formulation considerably overestimated α_{O_2} and did not account for the effect that Hct has on the amount of O₂ that can dissolve in blood. We refer to this model for the susceptibility of dissolved O₂ as the ideal gas model (IGM).

To account for the volume of dissolved O₂ and Hct, we consider the O₂ dissolved in each water compartment of blood—specifically, the water in plasma and the water in RBCs (18)—since quantities such as the partial molar volume of O₂ dissolved in water are well documented and enable direct calculation of the change of water volume as a function of pO₂. The details for calculating α_{O_2} and the relevant susceptibilities are given in Appendices A and B, respectively.

When the formulations for χ_{RBC} and χ_{plasma} from Spees et al. (13) are modified such that the susceptibilities of the contributing components are all expressed using volume susceptibilities and the contribution from dissolved O₂ to the water compartment is added, we get

$$\chi_{\text{RBC}} = \alpha_{\text{Hb}} \chi_{\text{diamHb}} + (1 - \alpha_{\text{Hb}})((1 - \alpha_{\text{O}_2})\chi_{\text{H}_2\text{O}} + \alpha_{\text{O}_2} \cdot \chi_{\text{O}_2}) + (1 - \text{SbO}_2) \cdot \Delta\chi_{\text{do}} \quad [3]$$

and

$$\chi_{\text{plasma}} = \alpha_{\text{prot}} \chi_{\text{prot}} + (1 - \alpha_{\text{prot}})((1 - \alpha_{\text{O}_2})\chi_{\text{H}_2\text{O}} + \alpha_{\text{O}_2} \cdot \chi_{\text{O}_2}). \quad [4]$$

In Eq. [3], α_{Hb} is the intracellular volume fraction of Hb and is equal to 0.266 (13), χ_{diamHb} represents the diamagnetic contribution to the susceptibility from each Hb molecule, regardless of oxygenation state; $\Delta\chi_{\text{do}}$ represents the susceptibility difference between fully oxygenated and fully deoxygenated RBCs (ignoring dissolved O_2); and SbO_2 is the fractional O_2 saturation of Hb. In Eq. [4], χ_{prot} is the susceptibility of plasma proteins; and α_{prot} , the volume fraction of plasma proteins, is given by the product $w_{\text{prot}} \rho_{\text{plasma}} \bar{v}_{\text{prot}} = 0.052$, where $w_{\text{prot}} = 0.07$ is the assumed mass fraction of proteins in plasma (13), $\rho_{\text{plasma}} = 1.026 \text{ g/cm}^3$ (19), and $\bar{v}_{\text{prot}} = 0.730 \text{ cm}^3/\text{g}$ is the partial specific volume of plasma proteins (19).

METHODS

Susceptibility measurements were made in oxygenated samples of distilled water as well as ex vivo bovine plasma in a large water phantom for imaging. Details of the methods are given below.

Sample Preparation

Distilled water was used for the experiments in water, and ex vivo bovine plasma (GeneTex, Inc., Irvine, CA) was used for the plasma experiments. The plasma composition was 8 g/dL of protein, a molality of 174.5 mmol/kg, <2 mg/dL of Hb, and 8 g/L of trisodium citrate (Na-citrate) anticoagulant. All measurements were conducted at room temperature.

For each water and plasma measurement, a 50-mL centrifuge tube was filled three-quarters full with the liquid and sealed with a rubber septum and self-adhesive film. O_2 was bubbled through the liquid at a low flow rate (< 5 L/min) for 0 to 10 minutes using a catheter connected to a medical O_2 supply.

After bubbling, the sample was gently agitated to ensure uniform oxygenation. The oxygenated liquid was transferred via syringe to a 120-mm, 15-mL polypropylene centrifuge tube with a 17-mm outer diameter that was also sealed with a rubber septum and self-adhesive film. Another needle was inserted into the tube such that as much air as possible could be expelled prior to imaging it.

Immediately after the transfer, the sample was imaged while the pO_2 of the remaining liquid in the large centrifuge tube was measured. pO_2 measurements were made with an Orion Star A323 dissolved O_2 meter connected to a photo-luminescence pO_2 probe (Thermo Fisher Scientific Inc., Waltham, MA).

MR Susceptometry

To measure the susceptibility of the samples, we used the relation between the susceptibility difference inside

and outside the tube, $\Delta\chi = \chi_{\text{in}} - \chi_{\text{out}}$, to the Larmor frequency shift inside the tube, Δf_0 , by approximating the tube as an infinite cylinder (20):

$$\Delta f_0 = \frac{1}{6} \Delta\chi f_0 (3\cos^2\theta - 1), \quad [5]$$

where f_0 is the center frequency, and θ is the angle the tube makes with the external field, B_0 . For small θ , the field offset outside of the tube is negligible.

Based on our theory, the expected difference in susceptibility between plasma at a pO_2 of 110 mm Hg (at normoxia) and at 550 mm Hg (upper range of hyperoxia challenges) is approximately 24 ppb. Using Eq. [5] with the tube aligned parallel to B_0 , this change in susceptibility would result in a frequency shift of only 1 Hz at 3 Tesla (T); therefore, the imaging protocol was designed to be sensitive to frequency shifts with a precision < 0.1 Hz.

To measure the frequency shifts across the phantom, we used multiecho gradient-recalled echo (GRE) imaging and the linear relation between phase and frequency over time:

$$\phi(x, y, t) = 2\pi\Delta f_0(x, y) \cdot t + \phi_0(x, y), \quad [6]$$

where $\phi(x, y, t)$ is the phase at time t at the voxel with coordinates (x, y) and ϕ_0 is the phase offset immediately after excitation at that voxel.

MRI Data Acquisition

All imaging was on a 3 T Siemens TIM Trio system (Siemens, Erlangen, Germany) using the vendor-supplied 32-channel receive-only head coil. The prepared sample was placed along the axis of a plastic 4-L cylindrical phantom filled with distilled water as a reference medium while two poly(methyl methacrylate) (PMMA) inserts held the tube in place by its ends. The phantom was positioned in the head coil with the tube aligned parallel to the B_0 field. A single slice, two-dimensional (2D) multiecho GRE sequence with monopolar readout was used for imaging. A 5-mm axial slice centered on the midpoint of the tube was acquired on a 256×256 matrix over a $200 \times 200 \text{ mm}^2$ field of view. Imaging parameters were: 16 echoes, first echo time (TE) of 3.0 ms, 3.75-ms echo spacing, 500 Hz/pixel readout bandwidth, and a 90-ms repetition time (TR). The total acquisition time was 23 s. Prior to running the sequence, Siemens advanced shimming was performed on the slice.

For the plasma samples only, forcing all of the air bubbles out of the tubes was sometimes not possible; in this case, the phantom was tilted upward slightly in order to shift the bubbles away from the imaging slice. For all plasma samples, therefore, an additional low-resolution 2D multislice GRE scan was acquired such that the tube angle could be measured on the magnitude images. This scan used the same imaging parameters as the single slice acquisition above, except that it used 20 5-mm slices with a 1-mm slice gap, a 128×128 matrix, a single echo time with TE = 20 ms, and a 500 ms TR.

Image Processing

All image processing was performed in MATLAB (The MathWorks Inc., Natick, MA). To accurately generate

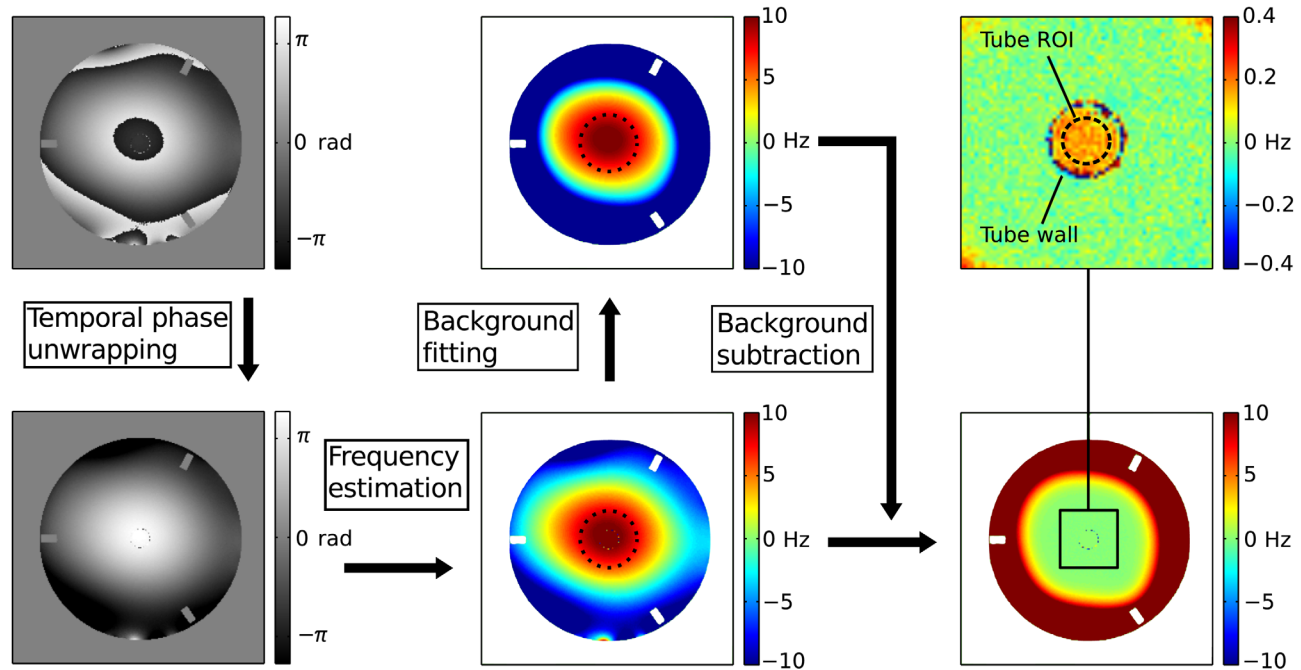


FIG. 1. Schematic overview of the field mapping pipeline on a water sample going from raw phase images to background-corrected frequency maps (see the Methods section for a detailed description of the steps). The dotted black circle on the frequency maps in the center column represents the boundary of the inclusion ROI within which the background field mapping was performed. The top right is a zoom-in of the background-corrected field map, with the windowing adjusted to highlight the frequency difference inside and outside the tube. The dashed black circle within the zoom-in represents the boundary of the ROI in the tube over which the frequency values were averaged for determining $\Delta\chi$ with Eq. [5].

phase images for each echo, we reconstructed individual channel images using the multichannel recombination method introduced by Robinson et al. (21). We adapted their implementation to our data by using all 16 echoes at the full spatial resolution of the acquisition. The offset-corrected images were bound between $\pm\pi$ and were saved for processing in the main pipeline. Magnitude images were output from the scanner using sum of squares reconstruction.

To calculate $\Delta\chi$ from the magnitude and offset-corrected phase images, the following steps were performed: temporal phase unwrapping, field map estimation, background field removal, and susceptibility calculation. These steps are summarized in Figure 1. First, the phase images were temporally unwrapped such that the phase values were no longer bound between $\pm\pi$. For the n -th echo, this was done by adding the phase of the product of the n -th complex image and the complex conjugate of the $(n-1)$ -th complex image to the phase of the previously unwrapped image. The phase of the first echo was left unmodified.

After phase unwrapping, a field map, Δf_{meas} , was estimated by linearly fitting the phase over time on a voxel-wise basis using weighted least-squares. The squared magnitude image values were used as the fit weights (22). The frequencies were given by the linear coefficients of the fits and maps of their estimated uncertainties, $\sigma_{\Delta f}$, were also produced.

To correct for macroscopic field inhomogeneities, Δf_{inhom} , a retrospective background field estimation method was used (23). In the original method, a second-

order 2D polynomial was fit to the field map across the entire phantom using weighted least-squares and subtracted from Δf_{meas} to produce a corrected map, Δf_{corr} . Prior to fitting, regions of interest (ROIs) covering the tubes and the voxels whose values in the magnitude image were below a certain threshold were masked out such that the fit would not be influenced by the offset of interest in the tube and by unreliable frequency measurements, respectively.

In our study, we found that fitting Δf_{inhom} across the entire phantom with a 2nd-order 2D polynomial did not satisfactorily remove the inhomogeneity in the region of the tube because large frequency fluctuations near the phantom wall tended to skew the fit. Therefore, we tested higher-order fits and restricted the fit to a 55-mm diameter inclusion ROI that was just over three times the diameter of the tube (as shown in the center column of Figure 1). A 6th-order 2D polynomial gave Δf_{corr} closest to 0, the lowest variance, and the highest adjusted coefficient of determination (R^2) of the fits when the phantom and the tube were both filled with distilled water and when no tube was present at all. To exclude voxels with low signal from the fit, a threshold corresponding to the maximum signal from any voxels with partial voluming with the tube wall was used. The weighting values for each voxel in the fit were given by $1/(\sigma_{\Delta f} + \lambda)^2$, where $\lambda = 1.6 \times 10^{-2}$ Hz prevented division by zero.

For each sample, Δf_{corr} at the center of the tube was averaged over a 12-voxel diameter ROI, giving $\overline{\Delta f}_{\text{corr}}$ (ROI represented by the dashed black circle in the top-right field map in Figure 1). For the plasma samples, the

tilt angle, θ , of the tube was measured by selecting three points along the axis of the tube on the low-resolution multislice image and then calculating the angle between the line of best fit through the points and B_0 . Finally, $\Delta\chi$ was calculated from Eq. [5] using $\Delta f = \overline{\Delta f}_{\text{corr}}$, the measured value of θ for plasma or $\theta = 0$ for water, and f_0 from the scanner (stored in the image headers). The uncertainty on $\Delta\chi$, $\sigma_{\Delta\chi}$, was estimated using standard error propagation methods with $\sigma_{\overline{\Delta f}_{\text{corr}}}$ equal to the standard deviation of Δf_{corr} in the tube ROI and $\sigma_\theta = 0.5^\circ$ for all samples, including water.

We tested the validity of the background field removal and susceptibility calculation by performing Fourier-based forward field modeling on a digital representation of our phantom (24–26) using realistic susceptibility values for all the materials (27). After fitting the generated background field to a 6th-order polynomial and subtracting this fit, the relationship between the remaining field shift inside the tube and the susceptibility difference between the liquid inside the tube and outside the tube agreed with the infinite cylinder model to within 0.1% when the tube angle relative to B_0 was varied from 0 to 5° . This was in agreement with other studies examining the range of validity of the infinite cylinder model (28,29).

Analysis

The measured values of $\Delta\chi$ in water and plasma were compared with the theory presented above using the pO_2 and temperature measurements from the oxygenated samples to calculate χ inside the tube, χ_{in} , and from the distilled water in the phantom to calculate χ in the surrounding water, χ_{out} . Equation [4] for χ_{plasma} was used for the calculations of both χ_{in} and χ_{out} : for the bovine plasma, α_{prot} was given by the product [protein] $\cdot \bar{v}_{\text{prot}} = 0.08 \text{ g protein/cm}^3 \text{ plasma} \times 0.730 \text{ cm}^3 \text{ plasma/g protein} = 0.058$; and for water, α_{prot} was set to 0. For each set of measurements, the line of best fit for $\Delta\chi$ vs. pO_2 was found using a general least-squares approach that incorporated the uncertainty in both the pO_2 and $\Delta\chi$ measurements (30). Differences between the measured and theoretically predicted slopes of $\Delta\chi/pO_2$ were tested for statistical significance using a two-tailed t test. Additionally, the measured slopes in all three solutions were themselves compared for statistical differences using an analysis of covariance (ANCOVA) test.

Because the original model for χ_{blood} (13) did not use anticoagulant, nor did it account for the susceptibilities of electrolytes, an offset between the measured susceptibility in plasma and the theoretical predictions from Eq. [4] was present. To account for this offset, we incorporated electrolytes and Na-citrate into our calculations by assuming that they also dissolve in the water compartment of Eq. [4].

To account for Na-citrate, we measured its susceptibility in water using our technique described above, dissolving 8 g/L of it in distilled water (the same concentration as the bovine plasma). We also repeated our measurements of the effect of dissolved O₂ on the susceptibility of the Na-citrate solution by oxygenating the solution over a range of pO_2 values.

For the electrolytes, we assumed that Na^+ and Cl^- were the sole electrolytes contributing to the susceptibility because they constitute the majority of the electrolyte concentration in plasma (31). Given a total molality of 174.5 mmol/kg in the plasma samples, we varied the molality of sodium chloride (NaCl) from 0 to 175 mmol/kg and determined which value resulted in the susceptibility offset that matched the measurements.

Finally, because the solubility coefficient of blood, ϵ , that the IGM used was measured for whole blood with normal Hb concentrations (17), it was not possible to compare it directly to our measurements in water and plasma. Because ϵ was based on the volume that all the moles of O₂ dissolved in blood would occupy as an ideal gas at STP, as a means of comparing this theory to our measurements, we first calculated the mole fraction and volume fraction in water/plasma using our theory and then converted these using the ideal gas law to the volume fraction that O₂ would occupy if the same number of moles were in the gaseous state:

$$\alpha_{O_2, \text{IGM}} = \frac{\alpha_{O_2}}{\bar{v}_{M,O_2:H_2O}} \cdot \frac{R \cdot T_{\text{stp}}}{P_{\text{stp}}}, \quad [7]$$

where $R = 82.06 \text{ (cm}^3 \text{ atm)/(mol K)}$ is the ideal gas constant, $T_{\text{stp}} = 273.15 \text{ K}$, $P_{\text{stp}} = 1 \text{ atm}$, and $\bar{v}_{M,O_2:H_2O}$ is the partial molar volume of O₂ dissolved in water. For this comparison, we calculated χ_{O_2} in the same manner as SD (16), described in Appendix B.

RESULTS

Oxygenating and scanning the samples was conducted at room temperature. The average temperature of the solutions was $(22 \pm 1)^\circ \text{C}$ for distilled water, $(23 \pm 1)^\circ \text{C}$ for distilled water with 8 g/L of dissolved Na-citrate, and $(21.92 \pm 0.08)^\circ \text{C}$ for plasma. The reason for the variation in temperature ranges was that the distilled water experiments were performed on multiple days, whereas the plasma samples were performed over several hours. The pO_2 and temperature of the water in the phantom was measured multiple times throughout the experiment, and the average values were $(151 \pm 3) \text{ mm Hg}$ and $(21.1 \pm 0.2)^\circ \text{C}$, respectively.

Using the multislice scans of the plasma samples, the average tilt angle of the tubes was $(1.4 \pm 0.8)^\circ$, with a maximum angle of 2.7° with respect to B_0 .

An example of the field mapping and background field removal for a scan of an oxygenated water sample is shown in Figure 1. In the inclusion ROI used for fitting the background field, the typical estimated uncertainty on the frequencies was approximately $(0.040 \pm 0.008) \text{ Hz}$, with a maximum uncertainty of 0.1 Hz; and inside the tube it was $(0.036 \pm 0.007) \text{ Hz}$, with a maximum uncertainty of 0.05 Hz. Therefore, this technique was capable of measuring frequency offsets with our specified precision $\leq 0.1 \text{ Hz}$ in our ROI.

Plots of $\Delta\chi$ versus pO_2 for all three solutions are shown in Figure 2. Also shown in Figure 2 are our model's predictions and the IGM's predictions for $\Delta\chi$ using the average temperature of each solution and the surrounding water in the phantom in the calculations of

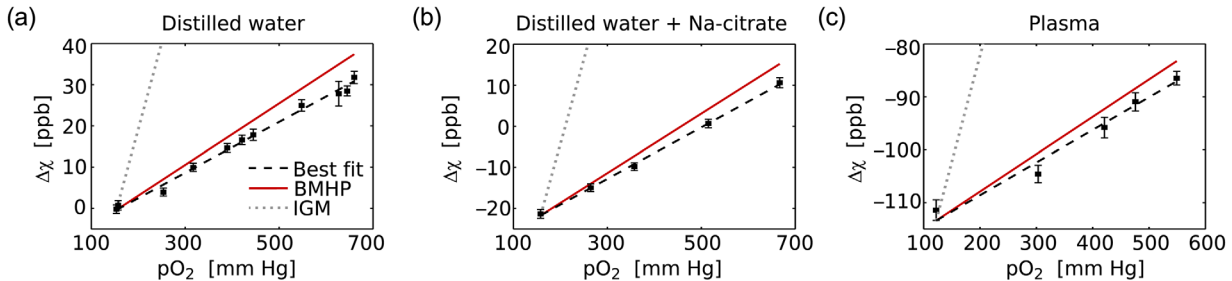


FIG. 2. Measured susceptibility differences (squares plus error bars) between oxygenated water (a), water + Na-citrate (b), and bovine plasma (c) and the surrounding water in the phantom. In each plot, the dashed black line is the line of best fit for the measurements; the solid red line is the predicted susceptibility difference using our (BMHP) theory; and the dotted grey line is the predicted susceptibility difference using the ideal gas model (IGM) employed by Schwarzbauer and Deichmann (16). To better compare the effect of dissolved O_2 , the vertical offsets of the theoretical predictions have been adjusted in the plots such that the lines intersect with the lines of best fit at normoxia. For clarity, the graphs' limits are constrained to the range of measured $\Delta\chi$ rather than the full range predicted by the IGM.

both. Note that in this figure, the $\Delta\chi$ offsets for the theoretical predictions have been adjusted such that the lines intersect with the lines of best fit at normoxia in order to best visualize the differences in $\Delta\chi/pO_2$ slopes. We have labeled our theory with our initials ‘‘BMHP’’.

The regression coefficients for the measured data are shown in Table 2, as well as the coefficients from our theory and the IGM. The far right column gives the coefficient of determination (R^2) for the lines of best fit; from these results and qualitatively from the plots in Figure 2, $\Delta\chi$'s dependence on pO_2 is obviously very linear for all three solutions.

From the $\Delta\chi$ measurements of distilled water with dissolved Na-citrate, we found the susceptibility of dissolved Na-citrate to be $\chi_{Na-cit} = (-12.1 \pm 0.2)$ ppm. For plasma, we used this value and tested the effect that dissolved Na-citrate and dissolved Na-citrate + NaCl had on the slope and offset of our theory. We found that the added solutes had no measurable effect on the slope but large effects on the offset. When both solutes were included in the model, 125 mmol NaCl/kg plasma was the molality that produced the offset best matching the measurements. This value is within an acceptable range, given a molality of 174.5 mmol/kg (31).

The most salient result was the discrepancy between the measured and modelled slopes of $\Delta\chi/pO_2$. We found that the IGM overestimated the slope by over 500%, whereas our theory produced a much more accurate prediction of the slope but still overestimated it by 14% to 21%. As demonstrated by the P -values in Table 2, the differences between the measured and our modelled slopes were statistically significant in water ($P = 2 \times 10^{-4}$) but not significant in water + Na-citrate or in plasma ($P = 0.06$ and 0.10, respectively). At a pO_2 of 550 mm Hg in plasma, these errors in the slopes translated into errors in the susceptibility of 145 ppb with the IGM and 4.5 ppb using our theory. When we compared the three measured $\Delta\chi/pO_2$ slopes from water, water + Na-citrate, and plasma using an ANCOVA test, there was no significant difference between the three of them ($P = 0.8$).

Finally, the high degree of linearity between $\Delta\chi$ and pO_2 would suggest that the detailed model presented here could be further simplified. This is because the vol-

ume fraction of O_2 , α_{O_2} , is extremely linear as a function of pO_2 , so we can express it as $\alpha_{O_2} = \epsilon' \cdot pO_2$, similar in form to the original IGM but with an empirically estimated constant of proportionality (ϵ'). Linearly fitting Eq. [A.1] versus pO_2 , we get $\epsilon' = 5.42 \times 10^{-8}$ mL O_2 /mL H_2O /mm Hg at 22 °C and 4.24×10^{-8} mL O_2 /mL H_2O /mm Hg at 37 °C. Based on the measured slopes of $\Delta\chi/pO_2$, the corresponding values of χ_{O_2} to use would be (1140 ± 60) ppm at 22 °C and (1090 ± 50) ppm at 37 °C using Curie's law.

DISCUSSION

Here, we have introduced a new model for the susceptibility of blood that incorporates dissolved O_2 in the water compartments of blood, and we have measured the change in susceptibility of plasma as a function of increasing pO_2 . Previous studies have already evaluated the change in χ_{blood} for whole blood with pO_2 ranging from 0 up to ~ 120 mm Hg (13,32). The work presented here complements these studies by considering the change in χ_{blood} over the hyperoxia range 120 mm Hg $< pO_2 < 600$ mm Hg. Plasma, rather than whole blood, was used here in order to disentangle dissolved O_2 -induced susceptibility changes from Hb-induced susceptibility changes.

We found that the IGM for the susceptibility of dissolved O_2 dramatically overestimated the change in susceptibility in all three of the solutions that we studied. This was due to the overestimation of the volume fraction of dissolved O_2 , as described in the Theory section and Appendices A and B. Our model was in much better agreement with the measurements, although it did slightly, but statistically significantly, overestimate the slope of $\Delta\chi/pO_2$ for water. We speculate that two separate factors may be contributing to the slightly decreased slope. The first is that, whereas Curie's law is sufficient for modelling the change in susceptibility for most paramagnetic molecules of interest in MRI, diamagnetic contributions to the susceptibility of O_2 from pairwise intermolecular interactions are greater with increasing molar density (33). Our estimate of χ_{O_2} may not have fully accounted for the diamagnetic contribution because

Table 2

The Coefficients of the Linear Fits of the Measured and Theoretical Changes in $\Delta\chi$ Versus pO₂ Using Our Theory^a and the IGM. Fits Are of the Form $\Delta\chi = m_{\Delta\chi} \times pO_2 + \Delta\chi_0$

Solution	$m_{\Delta\chi}$ (ppb/ mm Hg)	$m_{\Delta\chi}\%$ Difference	t Test (P)	$\Delta\chi_0$ (ppb)	$\Delta\chi_0\%$ Difference	R^2
Water						
Measured	0.062 ± 0.002			-9.8 ± 0.8		0.993
BMHP	0.075	21	2×10^{-4}	-11	12	
IGM	0.42	580	3×10^{-17}	-65	560	
Water + Na-citrate						
Measured	0.063 ± 0.003			-32 ± 1		0.998
BMHP + 8 g/L Na-citrate	0.072	14	0.06	-32	0	
IGM	0.41	550	2×10^{-6}	-62	94	
Plasma						
Measured	0.062 ± 0.005			-121 ± 2		0.973
BMHP	0.071	15	0.09	-74.4	-39	
BMHP + 8 g/L Na-citrate	0.071	15	0.10	-95.4	-21	
BMHP + 8 g/L Na-citrate + 125 mmol/kg NaCl	0.071	15	0.10	-122	0.8	
IGM	0.40	550	7×10^{-6}	-129	7	

IGM, ideal gas model.

^aBMHP theory by Berman, Ma, Hoge, and Pike.

O₂ dissolved in liquid is actually at a much higher density than as a gas, and our reference value for χ_{O_2} was measured with O₂ in its gaseous state at 1 atm (34).

In addition to intermolecular interactions having a potential impact on the diamagnetic contribution to χ_{O_2} , there is evidence for O₂-H₂O interactions that may affect the paramagnetism of χ_{O_2} . Dissolved O₂ has been found to add another ultraviolet absorption band to the spectra of organic solvents, including water (35). It is believed that this is caused by a charge transfer effect in which O₂ behaves as an electron acceptor and the solvent molecules as electron donors. Given that O₂'s paramagnetic behavior is the result of it having two unpaired electrons, it is plausible that this charge transfer could fractionally reduce the effective number of unpaired electrons and therefore reduce the magnetic moment and paramagnetism of dissolved O₂. It is not clear how much each of the above two mechanisms contribute to the observed minor discrepancy between theory and experiment; it is beyond the scope of this study.

If we briefly reexamine how increased dissolved O₂ in arterial blood may affect T_2^* -weighted imaging, it is best to put it in perspective with the changes occurring in venous blood. If a subject has average resting physiological conditions with arterial pO₂ = 110 mm Hg, Hct = 0.4, and O₂ extraction fraction = 0.35, then the venous SbO₂ will be 0.65. If arterial pO₂ increases to 550 mm Hg under hyperoxia and changes in O₂ metabolism and blood flow are considered negligible, the venous SbO₂ will increase to 0.74 (7). Using our model for χ_{blood} at 37 °C with $\chi_{O_2} = 1,090$ ppm, as measured, the expected change in the susceptibility of arteries would be -5.3 ppb,* whereas the change in veins would be -127 ppb. The change is more than 20 times larger in venous blood than in arterial blood, meaning that any possible signal

change that may arise from $\Delta\chi$ in arteries would be dwarfed by the change resulting from veins. For comparison, the IGM predicted a change of +125 ppb in arteries. A scenario in which arterial susceptibility changes may actually contribute more noticeably would be in the event of scanning extremely anemic patients during hyperoxia. Performing the analysis above but with Hct = 0.2, $\Delta\chi$ for arteries is +7.1 ppb and for veins is -98 ppb. In this case, caution may be required when interpreting BOLD signal changes from hyperoxia. However, for most physiological conditions, hyperoxia-driven T_2^* contrast will be dominated by dHb in veins and capillaries.

CONCLUSION

We have presented a model for the susceptibility of blood that incorporates dissolved O₂, and we have experimentally validated the theory over a wide range of pO₂ values in distilled water and in plasma. We found that the change in susceptibility was marginally less than predicted, and we have characterized the observed solubility of dissolved O₂ in water and its susceptibility such that they can easily be incorporated into future modeling. Most important, in contrast to previous predictions that overestimated the volume fraction of dissolved O₂ (16), our results indicate that the effect of dissolved O₂ on the susceptibility of blood is negligible, even at the highest levels of hyperoxia. This work shows that, except in some extreme physiological circumstances, the susceptibility of dissolved O₂ can generally be ignored in MRI studies employing hyperoxia.

APPENDIX A

Here, we describe how we calculate the volume fraction of dissolved O₂ in water, α_{O_2} , for a given pO₂. α_{O_2} can be given by the product of the mole fraction of O₂ dissolved in water, \bar{n}_{O_2} , and the partial molar volume of O₂ dissolved in water, $\bar{v}_{M,O_2:H_2O}$, all divided by the total molar volume of the O₂-water solution:

*Arteries show a negative change in susceptibility because, at 110 mm Hg, SbO₂ is approximately 98%; and at 550 mm Hg, it increases to essentially 100%. Therefore, the change in susceptibility from the 2% dHb converting to oxy-Hb outweighs the positive change in susceptibility from the added dissolved O₂.

$$\alpha_{O_2} = \frac{\bar{n}_{O_2} \cdot \bar{v}_{M,O_2:H_2O}}{\bar{n}_{O_2} \cdot \bar{v}_{M,O_2:H_2O} + (1 - \bar{n}_{O_2}) v_{M,H_2O}}. \quad [A.1]$$

For the range of pO_2 encountered under normoxia and hyperoxia, the dissolved O_2 -water solution is very dilute; therefore, the molar volume of H_2O (v_{M,H_2O}) is used in place of the partial molar volume. \bar{n}_{O_2} is obtained by Henry's law using an empirical formula for the reference \bar{n}_{O_2} at atmospheric pressure (36):

$$\bar{n}_{O_2}(pO_2, T) = \exp\left(A + \frac{B}{(T + 273.15)}\right) + C \ln\left((T + 273.15) \cdot 100 \text{ K}^{-1}\right) \cdot \frac{pO_2}{760 \text{ mm Hg}}, \quad [A.2]$$

with $A = -66.7354$, $B = 8747.55 \text{ K}$, $C = 24.4526$, and T is the temperature in degrees Celsius. $\bar{v}_{M,O_2:H_2O}$ can be obtained empirically by the formula $\bar{v}_{M,O_2:H_2O}(T) = (31.7 - 0.04 \text{ }^\circ\text{C}^{-1} \cdot T) \text{ cm}^3/\text{mol}$ (37). Over the range of pO_2 explored in this study, the ratio of $\varepsilon \cdot pO_2/\alpha_{O_2}$ at $37 \text{ }^\circ\text{C}$ remains relatively constant at 731. For example, when $pO_2 = 500 \text{ mm Hg}$ and $T = 37 \text{ }^\circ\text{C}$, Eq. [A.1] gives a volume fraction for dissolved O_2 of 2.12×10^{-5} ; whereas in the IGM, $\varepsilon \cdot 500 \text{ mm Hg} = 1.55 \times 10^{-2}$.

To test the agreement of these calculations with the established solubility coefficient of O_2 in blood at STP, when α_{O_2} for a given pO_2 is converted back to the gaseous volume of O_2 relative to water volume using Eq. [7] and then converted to the gaseous volume of O_2 relative to blood volume using Eq. [5] from (17), we end up with a Bunsen solubility coefficient of O_2 in blood equal to $3.13 \times 10^{-5} \text{ mL } O_2/\text{mL blood/mm Hg}$. This is in perfect agreement with the original value given in (7,17).

APPENDIX B

Here, we describe in detail how the susceptibilities of several of the constituents of blood and our experimental samples were calculated.

As shown in Table 1, the molar susceptibility of O_2 is governed by Curie's law and is therefore inversely proportional to temperature. We converted to volume susceptibility by dividing the molar susceptibility by the partial molar volume of O_2 ; whereas in the IGM, the molar susceptibility was divided by the molar volume of gaseous O_2 at 1 atm and $37 \text{ }^\circ\text{C}$. The result is that χ_{O_2} is actually significantly larger in our model; and the product $\alpha_{O_2}\chi_{O_2}$ works out to be roughly the same for our two models. However, because α_{O_2} in the IGM is overestimated, the factor $(1 - \alpha_{O_2})$ significantly reduced the contribution of the remaining constituents of χ_{blood} .

For the susceptibility of water, it has been shown that there exists a slight temperature dependence, such that χ_{H_2O} is given by (38)

$$\chi_{H_2O}(T) = \frac{4\pi(-12.96 \times 10^{-6} \text{ cm}^3/\text{mol})}{v_{M,H_2O}(T)} \times (1 + D \cdot (T - 20) + E \cdot (T - 20)^2), \quad [B.1]$$

where $D = 1.38810 \times 10^{-4} \text{ }^\circ\text{C}^{-1}$, $E = -1.2685 \times 10^{-7} \text{ }^\circ\text{C}^{-2}$, and $4\pi(-12.96 \times 10^{-6}) \text{ cm}^3/\text{mol}$ is the molar susceptibility of H_2O at $20 \text{ }^\circ\text{C}$ (34). Spees et al. (13) did not

account for this temperature dependence; therefore, our values for χ_{H_2O} differ slightly.

In order to measure Na-citrate's susceptibility in distilled water and to incorporate this into the susceptibility of the plasma samples, the mole and volume fractions of Na-citrate in the samples were calculated using a molecular mass of 294.10 g/mol and a partial molar volume of $69.32 \text{ cm}^3/\text{mol}$ (39). Similarly, for NaCl we used a partial molar volume of $16.3 \text{ cm}^3/\text{mol}$ at $22 \text{ }^\circ\text{C}$ (40) to help convert the molality to a volume fraction and to convert from molar susceptibility to get a volume susceptibility of -23.2 ppm (34).

REFERENCES

- Pauling L, Coryell CD. The magnetic properties and structure of hemoglobin, oxyhemoglobin and carbonmonoxyhemoglobin. Proc Natl Acad Sci U S A 1936;22:210–216.
- Ogawa S, Tank DW, Menon R, Ellermann JM, Kim SG, Merkle H, Ugurbil K. Intrinsic signal changes accompanying sensory stimulation: functional brain mapping with magnetic resonance imaging. Proc Natl Acad Sci U S A 1992;89:5951–5955.
- Kwong KK, Belliveau JW, Chesler DA, et al. Dynamic magnetic resonance imaging of human brain activity during primary sensory stimulation. Proc Natl Acad Sci U S A 1992;89:5675–5679.
- Bandettini PA, Wong EC, Hinks RS, Tikofsky RS, Hyde JS. Time course EPI of human brain function during task activation. Magn Reson Med 1992;25:390–397.
- Reichenbach JR, Essig M, Haacke EM, Lee BC, Przetak C, Kaiser WA, Schad LR. High-resolution venography of the brain using magnetic resonance imaging. MAGMA 1998;6:62–69.
- Ogawa S, Lee TM, Nayak AS, Glynn P. Oxygenation-sensitive contrast in magnetic resonance image of rodent brain at high magnetic fields. Magn Reson Med 1990;14:68–78.
- Severinghaus JW. Simple, accurate equations for human blood O_2 dissociation computations. Journal of applied physiology 1979;46: 599–602.
- Chiarelli PA, Bulte DP, Wise R, Gallichan D, Jezzard P. A calibration method for quantitative BOLD fMRI based on hyperoxia. Neuroimage 2007;37:808–820.
- Mark CI, Fisher JA, Pike GB. Improved fMRI calibration: precisely controlled hyperoxic versus hypercapnic stimuli. Neuroimage 2011; 54:1102–1111.
- Blockley NP, Griffeth VE, Germuska MA, Bulte DP, Buxton RB. An analysis of the use of hyperoxia for measuring venous cerebral blood volume: comparison of the existing method with a new analysis approach. Neuroimage 2013;72:33–40.
- Pilkinton DT, Gaddam SR, Reddy R. Characterization of paramagnetic effects of molecular oxygen on blood oxygenation level-dependent-modulated hyperoxic contrast studies of the human brain. Magn Reson Med 2011;66:794–801.
- Yeung DK, Griffith JF, Li AF, Ma HT, Yuan J. Air pressure-induced susceptibility changes in vascular reactivity studies using BOLD MRI. J Magn Reson Imaging 2012;38:976–980.
- Spees WM, Yablonskiy DA, Oswood MC, Ackerman JJH. Water proton MR properties of human blood at 1.5 Tesla: magnetic susceptibility, T_1 , T_2 , T_2^* , and non-Lorentzian signal behavior. Magn Reson Med 2001;45:533–542.
- Yablonskiy DA, Sukstanskii AL, He X. Blood oxygenation level-dependent (BOLD)-based techniques for the quantification of brain hemodynamic and metabolic properties—theoretical models and experimental approaches. NMR Biomed 2013;26:963–986.
- Schenck JF. The role of magnetic susceptibility in magnetic resonance imaging: MRI magnetic compatibility of the first and second kinds. Med Phys 1996;23:815–850.
- Schwarzbauer C, Deichmann R. Vascular component analysis of hyperoxic and hypercapnic BOLD contrast. Neuroimage 2012;59:2401–2412.
- Roughton FJ, Severinghaus JW. Accurate determination of O_2 dissociation curve of human blood above 98.7 percent saturation with data on O_2 solubility in unmodified human blood from 0 degrees to 37 degrees C. J Appl Physiol 1973;35:861–869.
- Pittman RN. Regulation of tissue oxygenation. In: Granger DN, Granger JP, eds. Colloquium Series on Integrated Systems Physiology:

- From Molecule to Function to Disease. San Rafael, CA: Morgan & Claypool Life Sciences; 2009–2011.
19. van Slyke DD, Hiller A, Phillips RA, Hamilton PB, Dole VP, Archibald RM, Eder HA. The Estimation of Plasma Protein Concentration from Plasma Specific Gravity. *J Biol Chem* 1950;183:331–347.
 20. Ogawa S, Menon RS, Tank DW, Kim SG, Merkle H, Ellermann JM, Ugurbil K. Functional brain mapping by blood oxygenation level-dependent contrast magnetic resonance imaging. A comparison of signal characteristics with a biophysical model. *Biophys J* 1993;64:803–812.
 21. Robinson S, Grabner G, Witoszynskij S, Trattng S. Combining phase images from multi-channel RF coils using 3D phase offset maps derived from a dual-echo scan. *Magn Reson Med* 2011;65:1638–1648.
 22. Gudbjartsson H, Patz S. The Rician distribution of noisy MRI data. *Magn Reson Med* 1995;34:910–914.
 23. Langham MC, Magland JF, Floyd TF, Wehrli FW. Retrospective correction for induced magnetic field inhomogeneity in measurements of large-vessel hemoglobin oxygen saturation by MR susceptometry. *Magn Reson Med* 2009;61:626–633.
 24. Marques JP, Bowtell R. Application of a fourier-based method for rapid calculation of field inhomogeneity due to spatial variation of magnetic susceptibility. *Concept Magn Reson B* 2005;25B:65–78.
 25. Salomir R, De Senneville BD, Moonen CTW. A fast calculation method for magnetic field inhomogeneity due to an arbitrary distribution of bulk susceptibility. *Concept Magn Reson B* 2003;19B:26–34.
 26. Cheng YC, Neelavalli J, Haacke EM. Limitations of calculating field distributions and magnetic susceptibilities in MRI using a Fourier based method. *Phys Med Biol* 2009;54:1169–1189.
 27. Wapler MC, Leupold J, Dragonu I, von Elverfeld D, Zaitsev M, Wallrabe U. Magnetic properties of materials for MR engineering, micro-MR and beyond. *J Magn Reson* 2014;242:233–242.
 28. Langham MC, Magland JF, Epstein CL, Floyd TF, Wehrli FW. Accuracy and precision of MR blood oximetry based on the long paramagnetic cylinder approximation of large vessels. *Magn Reson Med* 2009;62:333–340.
 29. Li C, Langham MC, Epstein CL, Magland JF, Wu J, Gee J, Wehrli FW. Accuracy of the cylinder approximation for susceptometric measurement of intravascular oxygen saturation. *Magn Reson Med* 2012;67:808–813.
 30. Williamson JH. Least-Squares Fitting of a Straight Line. *Can J Phys* 1968;46:1845–1847.
 31. Jackson PGG, Cockcroft PD. Appendix 3: Laboratory Reference Values: Biochemistry. In *Clinical Examination of Farm Animals*. Malden, MA: Wiley-Blackwell; 2002. pp 303–305.
 32. Jain V, Abdulmalik O, Probert KJ, Wehrli FW. Investigating the magnetic susceptibility properties of fresh human blood for noninvasive oxygen saturation quantification. *Magn Reson Med* 2012;68:863–867.
 33. May EF, Moldover MR, Schmidt JW. Electric and magnetic susceptibilities of gaseous oxygen: Present data and modern theory compared. *Phys Rev A* 2008;78:032522.
 34. Magnetic susceptibility of the elements and inorganic compounds. In: Haynes WM, ed. *CRC Handbook of Chemistry and Physics*. 93rd ed. Boca Raton, FL: CRC Press/Taylor and Francis; Internet version, 2013.
 35. Tsubomura H, Mulliken RS. Molecular Complexes and Their Spectra .12. Ultraviolet Absorption Spectra Caused by the Interaction of Oxygen with Organic Molecules. *J Am Chem Soc* 1960;82:5966–5974.
 36. Solubility of selected gases in water. In: Haynes WM, editor. *CRC Handbook of Chemistry and Physics*. 93rd ed. Boca Raton, FL: CRC Press/Taylor and Francis; Internet version, 2013.
 37. Harvey AH, Kaplan SG, Burnett JH. Effect of dissolved air on the density and refractive index of water. *Int J Thermophys* 2005;26:1495–1514.
 38. Philo JS, Fairbank WM. Temperature-dependence of the diamagnetism of water. *J Chem Phys* 1980;72:4429–4433.
 39. Apelblat A, Manzurola E. Apparent molar volumes of organic-acids and salts in water at 298.15 K. *Fluid Phase Equilib* 1990;60:157–171.
 40. Millero FJ. Apparent and partial molar volume of aqueous sodium chloride solutions at various temperatures. *J Phys Chem* 1970;74:356–362.